

Electronic Supplementary Information

How an angstrom-thick oxide overcoat enhances durability and activity of nanoparticle-decorated cathodes in solid oxide fuel cells

Haoyu Li,^a Hung-Sen Kang,^a Simranjit Grewal,^b Art J. Nelson,^c Shin Ae Song^d and Min Hwan Lee^{*,a,b}

^a *Department of Mechanical Engineering, University of California, Merced, 5200 N. Lake Rd. Merced, CA 95343, USA; *E-mail: mlee49@ucmerced.edu*

^b *Graduate Program in Materials and Biomaterials Science and Technology, University of California, Merced, 5200 N. Lake Rd. Merced, CA 95343, USA*

^c *Lawrence Livermore National Laboratory Livermore, CA 94550, USA*

^d *Micro/Nano Scale Manufacturing Group, Korea Institute of Industrial Technology, 143 Hangeulro, Sangnok-gu, Ansan, Gyeonggi Province 15588, Republic of Korea*

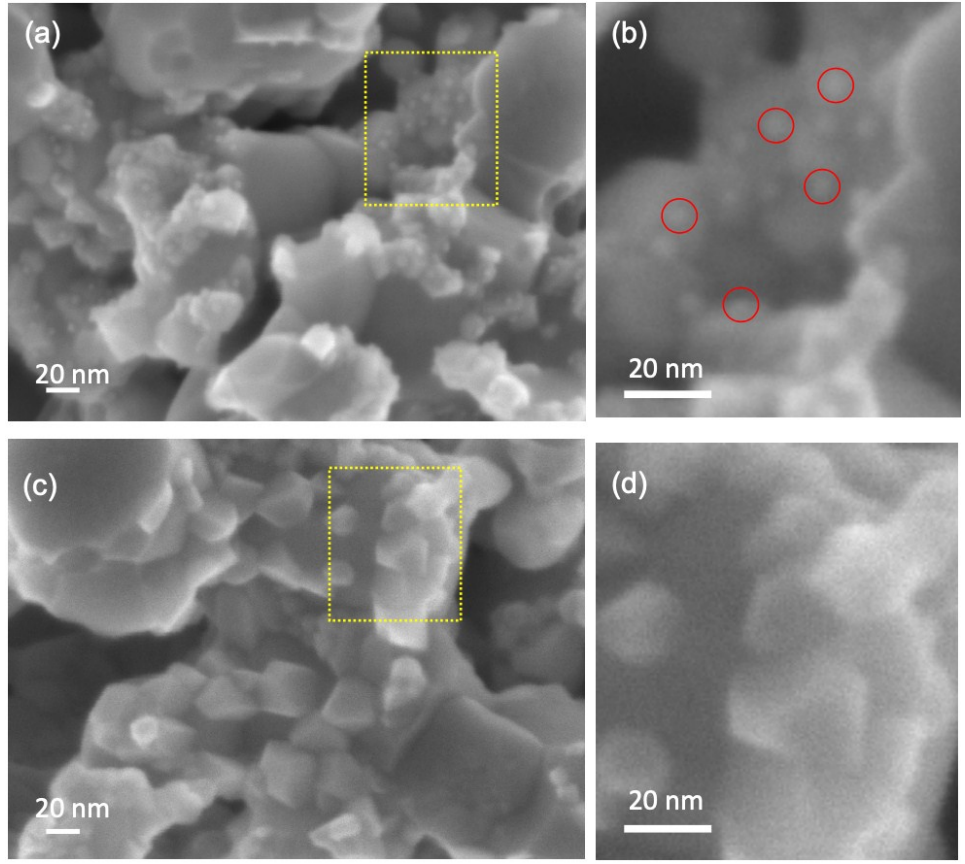


Fig. S1 SEM images of $\text{Ce}_{1\text{Inf-sint}}\text{Ce}_{\text{ALD6}}$ (a,b) and $\text{Ce}_{1\text{Inf-sint}}\text{Y}_{\text{ALD3}}$ (c,d) after 260 h at 700 °C. The dotted area in (a) is shown in (b). Some of ALD CeO_2 nanodots are circled in red.

Estimation of ALD growth rate

Ceria growth rate: There are several articles reporting the growth rate of ceria by ALD using tris(isopropylcyclopentadienyl)cerium(III) and H₂O as the precursor and oxygen source (the same as those used in this study). Wang et al. reported a CeO₂ film thickness of 1.3 nm after 80 ALD cycles on anatase TiO₂ nanoparticles at 250 °C, which is equivalent to ~ 0.163 Å per cycle.¹ Gupta et al. reported a ceria growth rate of 0.33 Å per cycle on a flat SiO₂ substrate at the chamber temperature of 250 °C.² While these two growth rates are within a reasonable proximity, majority others reported much higher growth rates of 2.5 – 3.0 Å per cycle.³ As Rahmanipour et al. noted, the measured growth rate varies widely dependent upon the geometry and surface chemistry of substrates and other deposition conditions.⁴ Herein, we quantified the ALD growth rate of our samples (by leveraging high-magnification SEM images) as shown below instead of simply relying upon prior reports.

In the zoomed-in SEM image of Ce_{Inf-sim}Ce_{ALD6} shown in Fig. S1a-b, the size of each ceria nanodots formed by ALD is ~ 3 nm in diameter. It is noted that only those deposited on infiltrated CeO₂ NPs (sized ~ 20 nm) forms nanodots while those deposited on the LNF backbone surface is not visible in the eyes of SEM. Therefore, we quantify the growth rate by focusing on the infiltrated CeO₂ NP region in Fig. S1b. With the aid of ImageJ software, we found that $\sim 7.3\%$ of the infiltrated CeO₂ surface is covered by the ALD-based ceria nanodots. Assuming the ceria nanodots are in a full sphere shape, we calculate the nominal thickness using the following simple relations.

$$A \cdot t = \left(\frac{4}{3}\pi r^3\right) \cdot N \dots\dots\dots (1)$$

$$(\pi r^2) \cdot N = 0.073 \cdot A \dots\dots (2)$$

where t , A , N and r corresponds to the nominal thickness (when assumed a uniform deposition), substrate surface area, total number of nanodots on a substrate of area A , and the radius of nanodots (1.5 nm). From this, we find the nominal ALD thickness of 1.46 Å. Since 6 cycles were performed to achieve this nominal thickness, the ceria growth rate is estimated to be ~ 0.24 Å per cycle.

Yttria growth rate: The aforementioned approach, however, could not be applied to our yttria deposition because there was not a localized morphological protrusion incurred by yttria ALD (Fig. S1d). Since the yttria growth rates reported by previous studies using the same precursor (tris(methylcyclopentadienyl)yttrium(III)), oxygen source (water) and chamber temperature (250 °C) are 0.8 – 3.5 Å per cycle on well-defined flat surfaces,⁵⁻⁷ which is within a similar range as those of ceria, we assume the same growth rate for yttria ALD on our porous electrode surface (i.e. 0.24 Å per cycle).

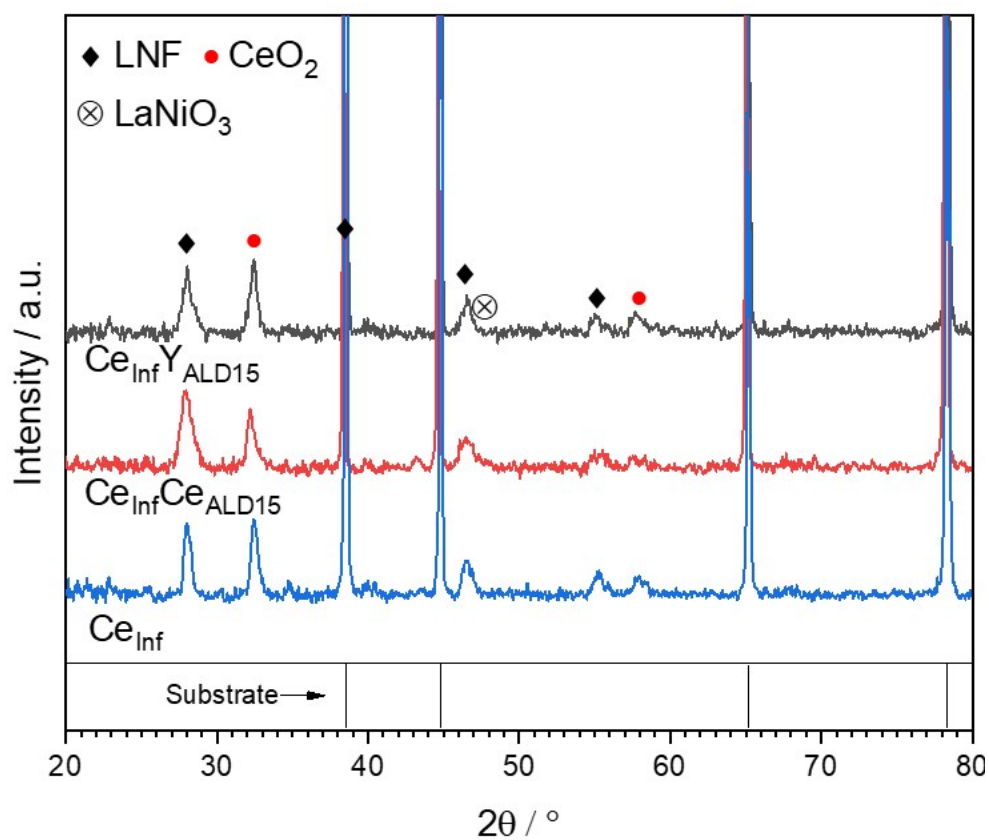


Fig. S2 XRD spectra of Ce_{Inf} , $\text{Ce}_{\text{Inf}}\text{Ce}_{\text{ALD15}}$ and $\text{Ce}_{\text{Inf}}\text{Y}_{\text{ALD15}}$ samples. Note that a much smaller amount of samples were placed on a substrate compared to the amount placed for Fig. 1i when performing XRD, resulting in a stronger peaks corresponding to the substrate.

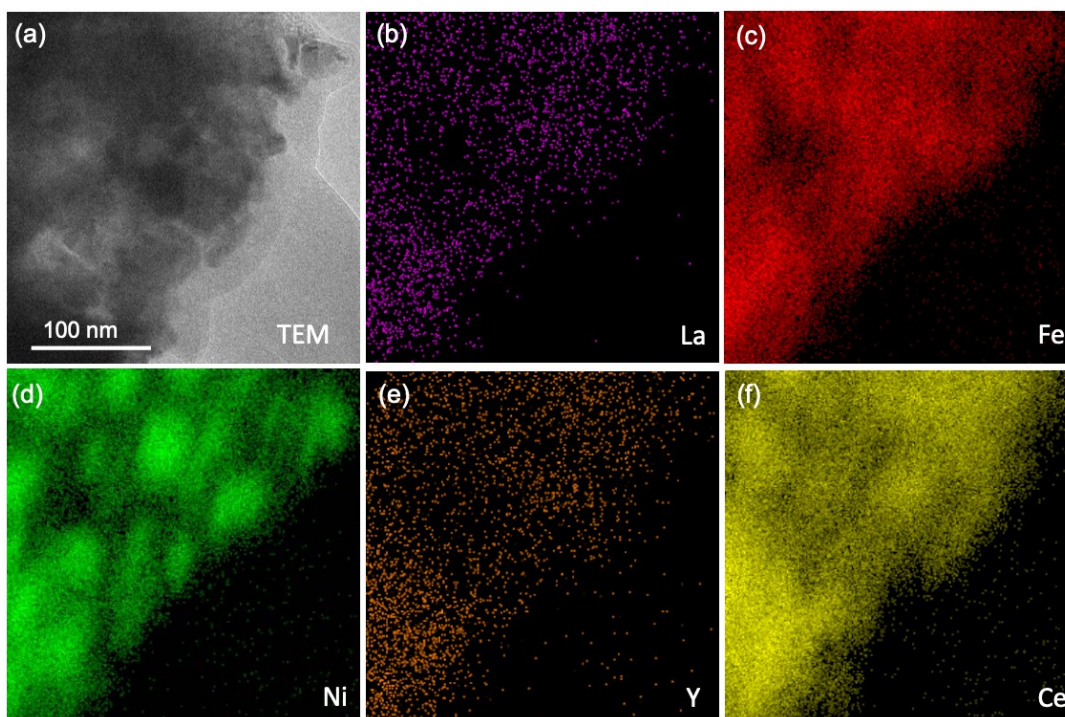


Fig. S3 A TEM image of $\text{Ce}_{\text{In}}\text{Y}_{\text{ALD15}}$ (a) and its corresponding EDS elemental mapping(b-f).

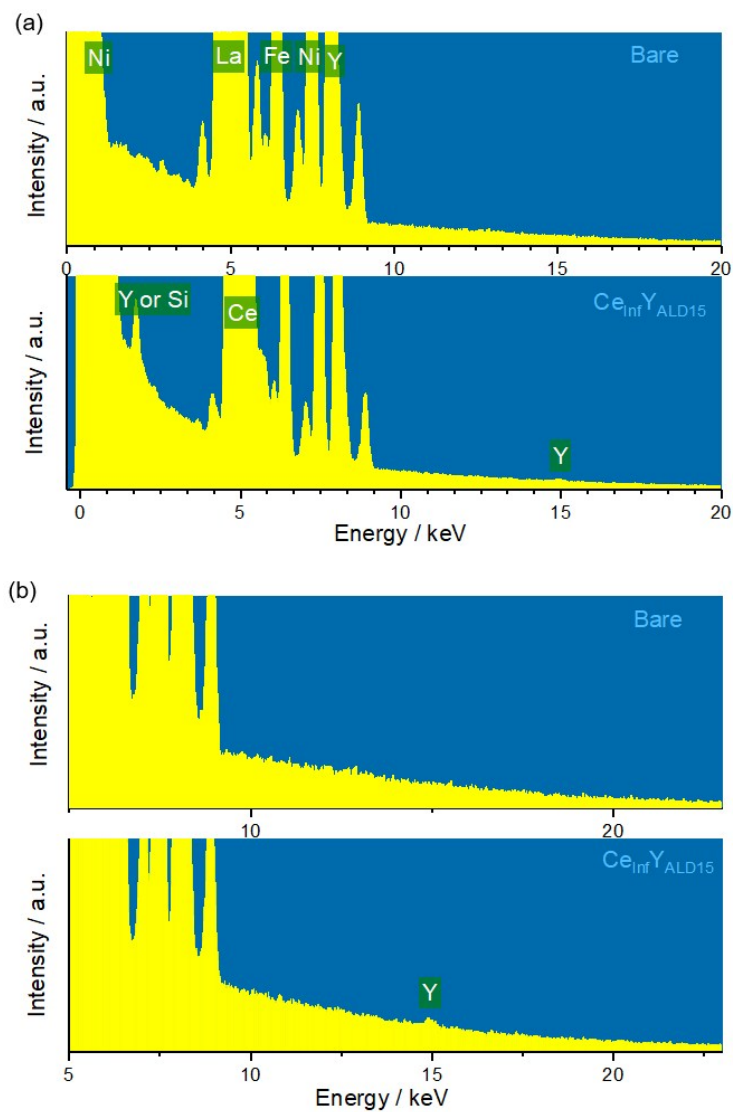


Fig. S4 EDS spectra of bare LNF and Ce_{Inf}Y_{ALD15} powder. (b) A zoomed-in y-axis to reveal the presence and absence of Y more explicitly.

Deconvolution of XPS spectra

Ce 3d: By taking the method by Maslakov et al.⁸ The fraction of Ce³⁺ and Ce⁴⁺ species from Ce 3d spectra was quantified by following relationship:

$$p(\text{Ce}^{3+}) = \frac{1 - \frac{3}{2}a_0\left(\frac{I_0}{I}\right)}{1 + \frac{3}{2}\left(\frac{I_0}{I}\right)} \quad \text{where} \quad a_0 = \frac{I_s}{\frac{3}{2}I_0}$$

$$I_0 = I(u_4), I_s = I(v_1) + I(v_3), I = I(v_0) + I(v_1) + I(v_2) + I(v_3)$$

$$p(\text{Ce}^{4+}) = 1 - p(\text{Ce}^{3+})$$

O 1s: Molar fraction of O-Ce³⁺ and O-Ce⁴⁺ from O 1s spectra was quantified by following relationship:

$$p(\text{O} - \text{Ce}^{3+}) = \frac{I(\text{O} - \text{Ce}^{3+})}{I(\text{O} - \text{Ce}^{3+}) + I(\text{O} - \text{Ce}^{4+})}$$

$$p(\text{O} - \text{Ce}^{4+}) = 1 - p(\text{O} - \text{Ce}^{3+})$$

Table S1. XPS Ce 3d peak analysis.

Peak	Ce_{inf}		Ce_{inf}Ce_{ALD6}		Ce_{ALD12}	
	B.E. [eV]	Area [a.u.]	B.E. [eV]	Area [a.u.]	B.E. [eV]	Area [a.u.]
u ₄	916.29	1028.51	916.29	1147.38	921.90	621.13
u ₃	906.91	994.63	907.22	1136.65	912.80	650.42
u ₂	903.40	136.24	902.90	410.89	908.40	156.86
u ₁	900.76	903.20	900.69	962.69	906.30	410.96
u ₀	899.10	49.19	899.10	57.50	904.10	104.65
v ₄	897.69	1542.77	897.70	1721.07	903.30	931.69
v ₃	888.44	1491.95	888.78	1704.97	894.38	975.62
v ₂	882.24	1354.79	882.15	1444.04	887.70	616.44
v ₁	884.18	204.37	884.3	616.33	890.20	235.30
v ₀	880.90	73.78	881.1	86.24	885.90	156.98
P(Ce ³⁺)		5.96%		12.6%		13.4%

Table S2. XPS O 1s peak analysis.

Peak	Ce_{Inf}		Ce_{Inf}Ce_{ALD6}		Ce_{ALD12}	
	B.E. [eV]	Area [a.u.]	B.E. [eV]	Area [a.u.]	B.E. [eV]	Area [a.u.]
O-Ce⁴⁺	528.6	2200.9	528.6	2562.0	528.5	1623.2
O-Ce³⁺	531.1	1320.2	531.1	1727.1	531.1	1514.2
Absorbed O₂	531.9	1099.3	532.0	1115.3	532.1	795.4
M-O	529.9	284.5	529.8	311.0	529.7	256.9
Ligand					534.8	276.4
p(O-Ce³⁺)		37.5%		40.2%		48.3%

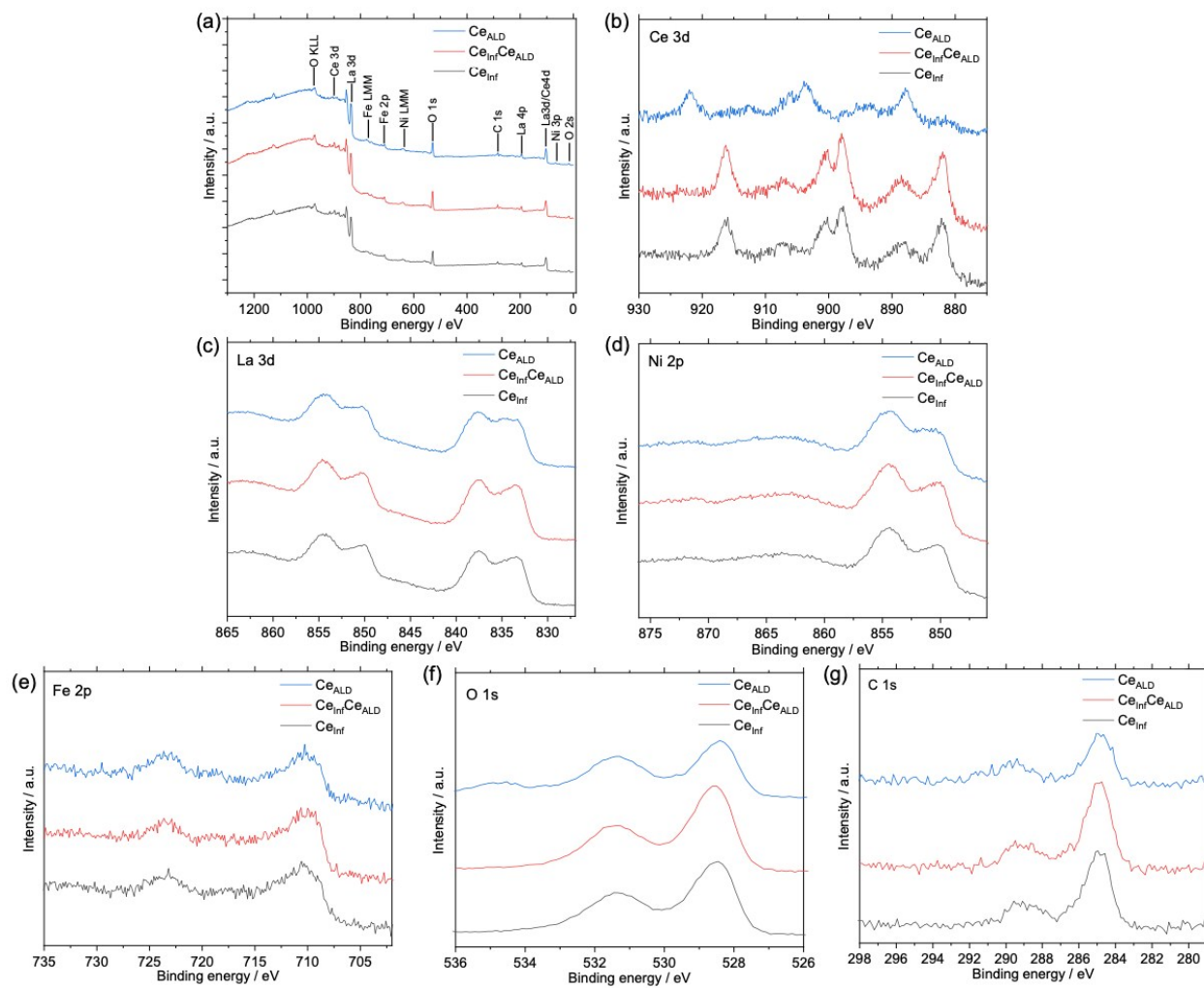


Fig. S5. XPS spectra. (a) Survey spectrum, (b) Ce 3d, (c) La 3d, (d) Ni 2p, (e) Fe 2p, (f) O 1s and (g) C 1s spectra.

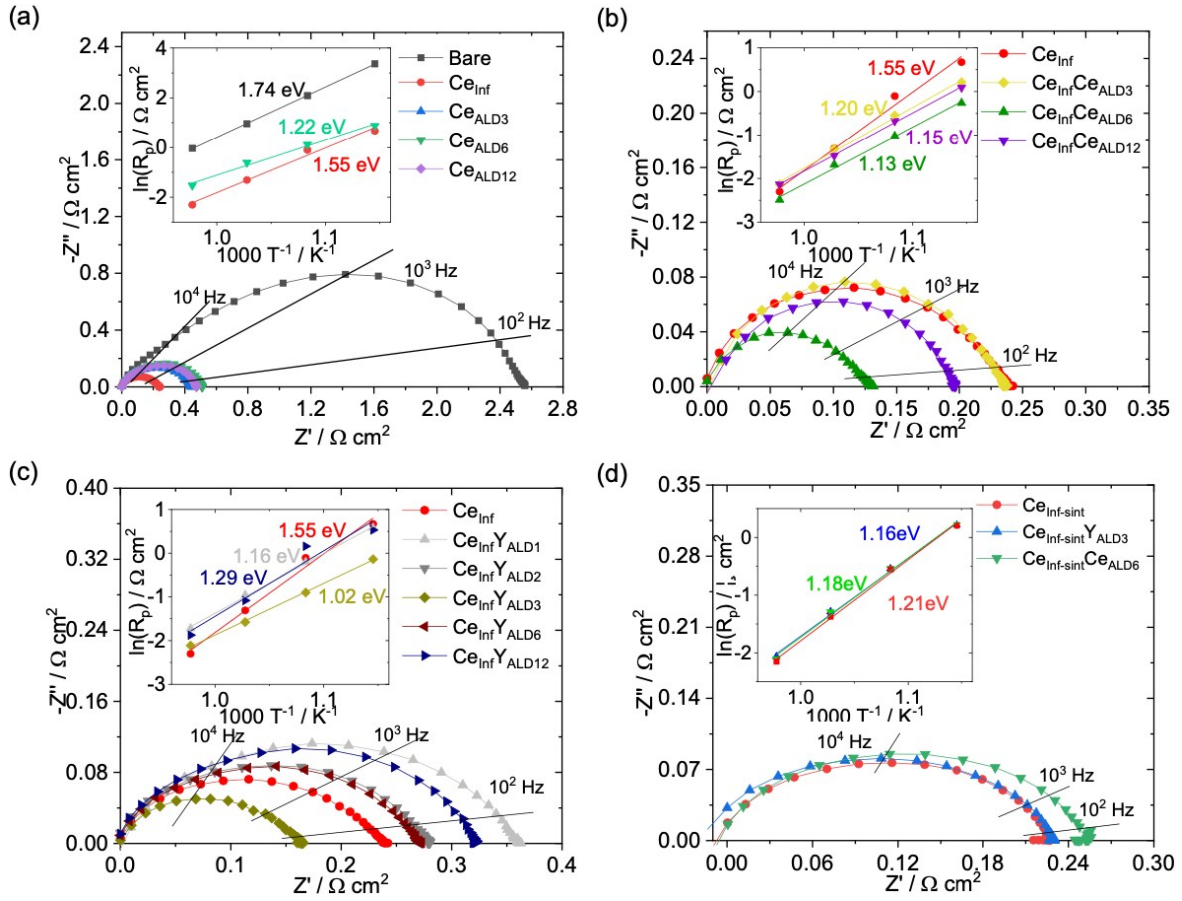


Fig. S6 EIS curves and Arrhenius plots (inset). In the insets, the activation energies (E_a) of each sample are calculated from the least square fitting of R_p values with temperature. (a) Bare, Ce_{Inf} and Ce_{ALDn} series, (b) $Ce_{Inf}Ce_{ALDn}$ series (c) $Ce_{Inf}Y_{ALDn}$ series and (d) the samples sintered before ALD ($Ce_{Inf-sint}Y_{ALD3}$ and $Ce_{Inf-sint}Ce_{ALD6}$).

EIS fitting to a single arc model

Most of EIS curves obtained for the study (except for those obtained at low oxygen activities as shown in Fig. S7 below) could be reasonably well fitted to a single arc-based $L-R_o-(R_p//Q_p)$ model. An additional low-frequency arc appears at low oxygen activities (< 0.1 atm), which is ascribed to a mass transport polarization. However, even at the lowest pO_2 in our study, the newly appearing arc is almost ten-fold smaller than the other main arc, and thus the corresponding R_p is negligible compared to the main R_p as shown in Fig. S7 in most cases. Therefore, we fitted all the presented data using the single arc-based model.

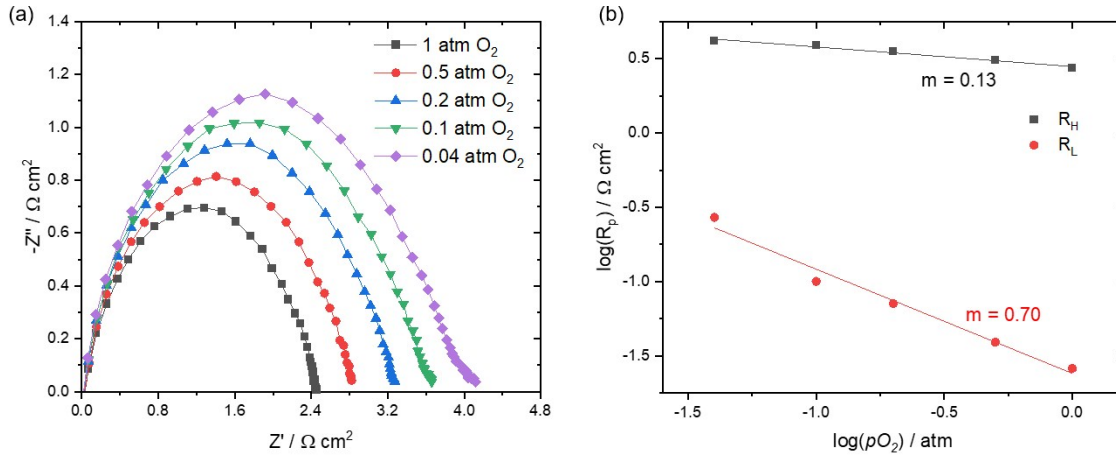


Fig. S7 (a) Nyquist plot of LNF bare sample obtained at various pO_2 and (b) corresponding polarization resistances versus pO_2 graph; here, the polarization resistances are acquired by fitting the EIS data to $R-L-R_o-(R_H//Q_H)-(R_L//Q_L)$. R_H and R_L corresponds to polarization resistances with higher and lower characteristic frequencies.

Table S3. Ohmic resistance (R_{ohm}), Polarization resistance (R_p) and their corresponding capacitance (C) calculated with CPE parameters (α and Q).

	R_{ohm} [Ω cm ²]	R_p [Ω cm ²]	α	Q [F s ^{1-α]}	C [F cm ⁻²]
Bare	1.37	2.73	0.77	2.4×10^{-4}	1.5×10^{-5}
Ce_{Inf}	0.92	0.27	0.63	4.41×10^{-3}	8.45×10^{-5}
Ce_{ALD6}	0.95	0.54	0.71	1.26×10^{-3}	6.41×10^{-5}
Ce_{Inf}Ce_{ALD6}	0.96	0.19	0.60	7.03×10^{-3}	8.52×10^{-5}
Ce_{Inf}Y_{ALD3}	0.82	0.21	0.62	4.44×10^{-3}	6.17×10^{-5}

Table S4. Summary of polarization resistances (R_p) at different temperatures and their activation energies (E_a).

	750 °C [$\Omega \text{ cm}^2$]	700 °C [$\Omega \text{ cm}^2$]	650 °C [$\Omega \text{ cm}^2$]	600 °C [$\Omega \text{ cm}^2$]	E_a [eV]
Bare	0.9683	2.7301	8.1029	28.9322	1.75
Ce_{Inf}	0.1001	0.2737	0.8983	1.9548	1.55
Ce_{Inf}Y_{ALD1}	0.1787	0.3848	0.814	1.7868	1.18
Ce_{Inf}Y_{ALD2}	0.1494	0.3115	0.6612	1.4096	1.15
Ce_{Inf}Y_{ALD3}	0.1208	0.2067	0.4065	0.8727	1.02
Ce_{Inf}Y_{ALD6}	0.1369	0.2912	0.6346	1.3697	1.18
Ce_{Inf}Y_{ALD12}	0.1534	0.3385	1.1723	1.6986	1.29
Ce_{Inf}Ce_{ALD3}	0.1179	0.2674	0.5784	1.2420	1.20
Ce_{Inf}Ce_{ALD6}	0.0828	0.1862	0.3598	0.7693	1.13
Ce_{Inf}Ce_{ALD12}	0.1183	0.2282	0.5093	1.0967	1.15
Ce_{ALD3}	0.2151	0.4956	1.3003	2.7843	1.33
Ce_{ALD6}	0.2172	0.5439	1.1261	2.4115	1.22
Ce_{ALD12}	0.2147	0.5087	1.0623	2.3993	1.22
Ce_{Inf-sint}	0.1164	0.2536	0.5749	1.2268	1.21
Ce_{Inf-sint}Y_{ALD3}	0.1270	0.2762	0.5819	1.2413	1.16
Ce_{Inf-sint}Ce_{ALD6}	0.1225	0.2756	0.5829	1.2481	1.18

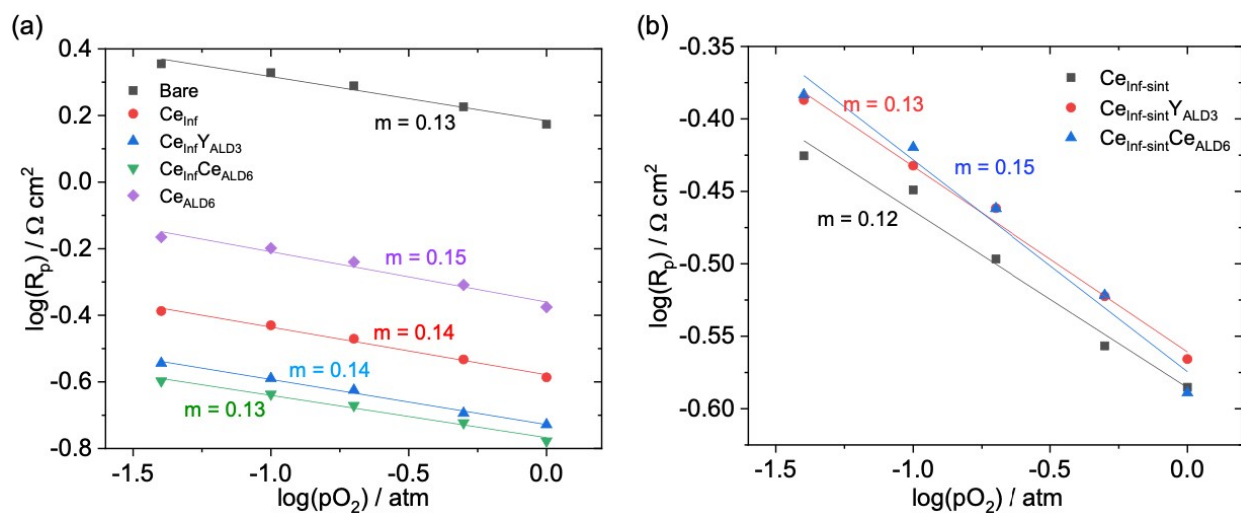


Fig. S8 Partial pressure dependency of polarization resistances measured at 700 °C.

Estimation of volumetric ratio

By taking the average size of infiltrated ceria NPs to be ~ 15 nm (see Fig. 6) and ALD growth rate of 0.24 Å per cycle, the volumetric ratio of ALD-deposited ceria or yttria nanodots ($V_{ALD} = 4\pi r_{Inf,NP}^2 \cdot t_{ALD}$ where V_{ALD} and t_{ALD} are the volume and nominal thickness of ALD-based film, and $r_{Inf,NP}$ is the radius of infiltrated ceria nanoparticles) to the infiltrated ceria ($V_{inf} = \frac{4}{3}\pi r_{inf}^3$ where V_{inf} is the volume of infiltrated ceria) is found to be $0.0048 \times (\text{number of ALD cycle})$. For example, considering a Type-III sample with 6 cycles of ALD, the volume of ALD-based ceria or yttria is 2.88% of infiltrated ceria volume ($0.0048 \times 6 = 0.0288$). Considering the amount of single-step infiltration forms $\sim 3\%$ of volume with respect to the LNF backbone,⁹ the amount of 6 cycle ALD-based ceria or yttria is only 0.087% of the backbone.

Effect of surface treatment on the RDS

The schematic diagram in Fig. S9 shows possible ORR pathways in the studied system. In this section, we discuss about what specific elemental step of ORR was dominantly affected by the surface treatment (infiltration and/or ALD) and how the treatment impacted the overall ORR kinetics. It is reminded that the reaction order (m) values of all the samples presented in Fig. 4 are 0.13 – 0.15 while the activation energies (E_a) and polarization resistances (R_p) become much smaller by a surface treatment.

The most sluggish step is often considered to be the bottleneck step (i.e. RDS), but this is the case only in a process where each step (sub-process) is arranged sequentially through a single route without a parallel pathway. In a process with parallel pathways, the most sluggish pathway may not be experimentally captured because the overall reaction rate will be determined by faster pathway(s) in this case. In our system, two different types of parallel pathways—bulk pathway (green) and surface pathway (yellow)—can be considered. Between the two, however, the bulk pathway is neglected (considered too resistive to compete against the surface pathway) based upon the following reasoning: (a) The extremely small concentration of oxygen vacancies in the LNF backbone should result in a negligible ionic conductivity,⁹⁻¹¹ and (b) the capacitance value measured from the EIS (on the order of 1×10^{-4} F cm⁻²) is too small to correspond to a bulk process.¹² Herein, we consider the surface pathways only (corresponding to **Steps 1 – 9** in Fig. S9). Among these, Steps 1, 2, 4, and 9 are not expected to have played a dominant role in enhancing the overall ORR kinetics by the surface treatment, and thus are not expected to comprise an RDS. The following lists the justification.

- **Step 1:** Since the overall microstructure (geometry/porosity) was rarely changed by the highly surface-specific treatments (infiltration and/or ALD), the mass transport of gaseous O₂ should not have been affected.
- **Step 2:** If the molecular adsorption step were the RDS, the reaction order (m) should be close to 1, but the m values of all the studied samples are much smaller than that (~ 0.15). In addition, the high-surface-area morphology of the LNF backbone (as opposed to a dense layer) should have provided abundant O₂ adsorption sites, making it even less likely to be an RDS.
- **Steps 4 and 9:** If the surface diffusion of the electroactive oxygen species (O or O⁻) were the RDS, m is expected to be close to 0.5. In addition, their slow kinetics (driven by diffusion) results in a low characteristic frequency (f_c), which is not aligned with the high f_c range we observe ($10^3 - 10^4$ Hz). Furthermore, specifically in the case of ceria infiltration, while the ceria infiltration (Ce_{Inf}) resulted in a significant decrease in R_p , the surface area where the infiltrated species occupy is only a small fraction of the whole LNF surface area, making it difficult to believe that the surface adatom diffusion is highly facilitated by the infiltrated particles.

Now, Steps 3, 5, 6, 7 and 8 are the remaining candidates. Among these, Steps 5, 6 and 7 are charge transfer reactions occurring at the TPB region where gas, cathode and electrolyte meet altogether. Although we cannot fully exclude the possibility of enhancing the electrochemical activity of TPB region by the surface treatment, it is unlikely to achieve 10-fold improvement in electrode performance by adding some additional ceria in the highly localized TPB region when considering the electrolyte material interfacing with the cathode is another ceria-based material (GDC). On the other hand, the majority of earlier studies report LSM and LNF are rate-limited by dissociation^{13–17} or dissociation with a charge transfer reaction.^{9,11} (Here, the similarity in the RDS between LSM and LNF is justified by their similar characteristics including extremely low oxygen vacancy concentration under operational oxygen activity, high activation energy for O₂ dissociation, and high electronic conductivity with negligible ionic conductivity.⁹) For these reasons, we conclude that **Steps 3 and 8 are responsible for the drastic improvement of overall electrode performance by the surface treatment, and the overall reaction rate is co-limited by dissociation and the subsequent partial reduction.**

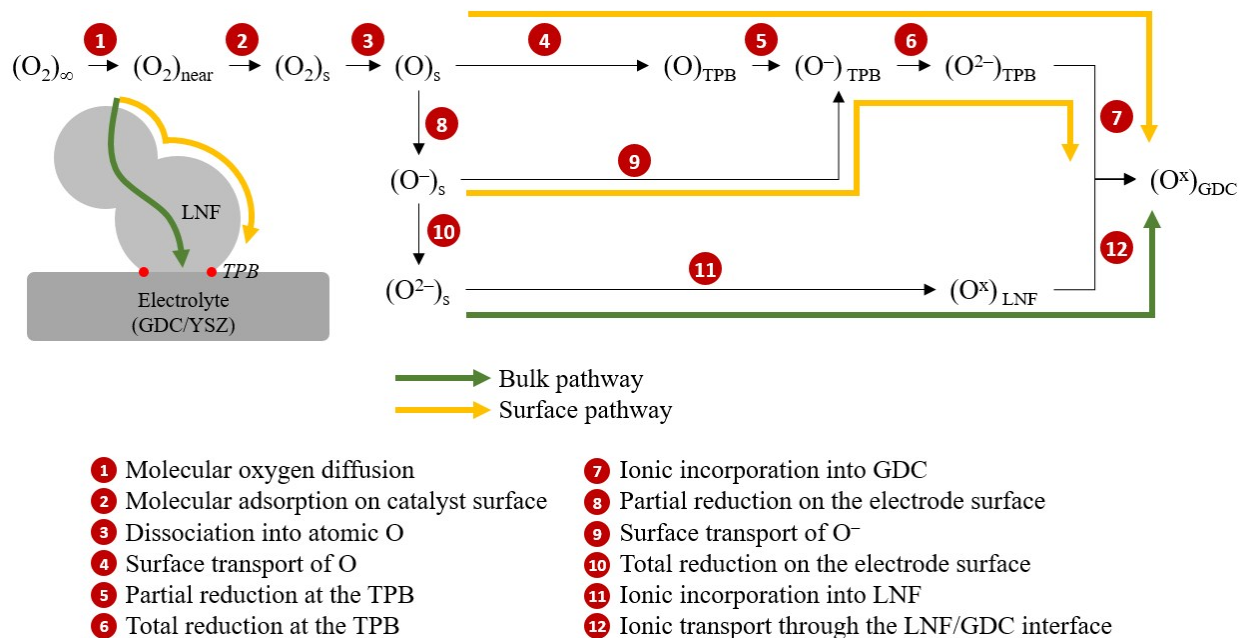


Fig. S9 A schematic diagram of possible ORR pathways in a LNF/GDC system. (O₂)_s and (O)_s refer to O₂ and O adsorbed on the electrode surface, respectively; TPB stands for triple phase boundary.

Quantification of infiltrated particle sizes

Assuming that the infiltrated ceria NPs form small islands not greater than half of the LNF backbone, the size of ceria particles was quantified for all the particle that is less than ca. 60 nm from $760 \times 520 \text{ nm}^2$ field emission SEM images. The SEM images that have ca. 200 or more of infiltrated NPs are chosen to provide a meaningful size distribution. As presented in Fig. S1b, we could resolve nanodots as small as 3 – 6 nm from images acquired from the same SEM system. The size of the ceria particles was obtained on a magnified version of the original SEM images by drawing a circle that fits best to the eyes with the perimeter of each infiltrated NP as presented in Fig. S10b, and denoting the diameter of the fitted circle. For a particle whose shape deviates significantly from a circle, the size was taken from the average between its longest length and the length in the direction perpendicular to the longest side. When estimating the size of each particle, a size with step of 3 nm were taken with error tolerance of $\pm 1.5 \text{ nm}$ (e.g. $3 \pm 1.5 \text{ nm}$, $6 \pm 1.5 \text{ nm}$, $9 \pm 1.5 \text{ nm}$, ...).

To test whether this method enables a convincing approximation, we applied this approach to two different SEM images from a specific sample ($\text{Ce}_{\text{Inf}}\text{Ce}_{\text{ALD6}}$) and presented the resulting distribution in Fig. S11. As demonstrated, not only the overall distribution (Fig. S11c) but also the d_{20} , d_{50} and d_{80} values from the two areas are in a close proximity (Fig. S11d).

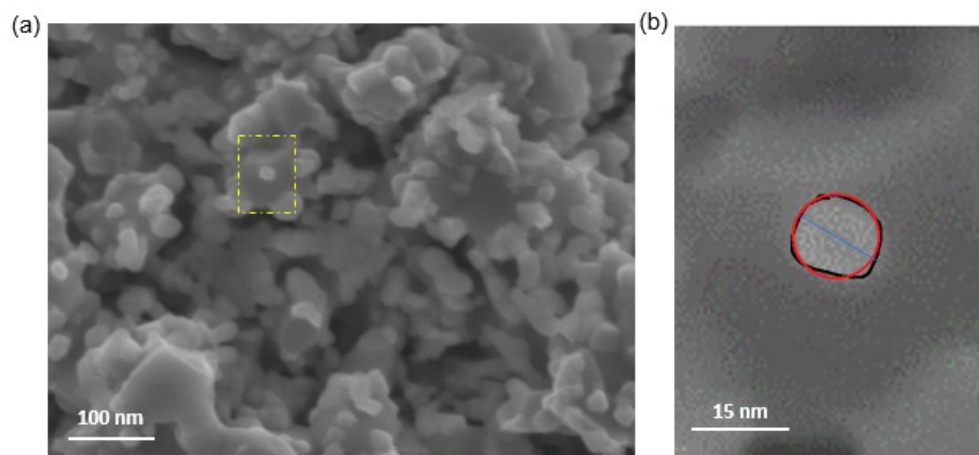


Fig. S10 (a) An exemplary SEM image taken from $\text{Ce}_{\text{Inf}}\text{Ce}_{\text{ALD6}}$ (a,b), and (b) a close-up image in the dotted area in (a). The size of the nanoparticle defined by the black line was estimated by drawing a red circle. The resulting diameter of the red circle was quantified as the particle size.

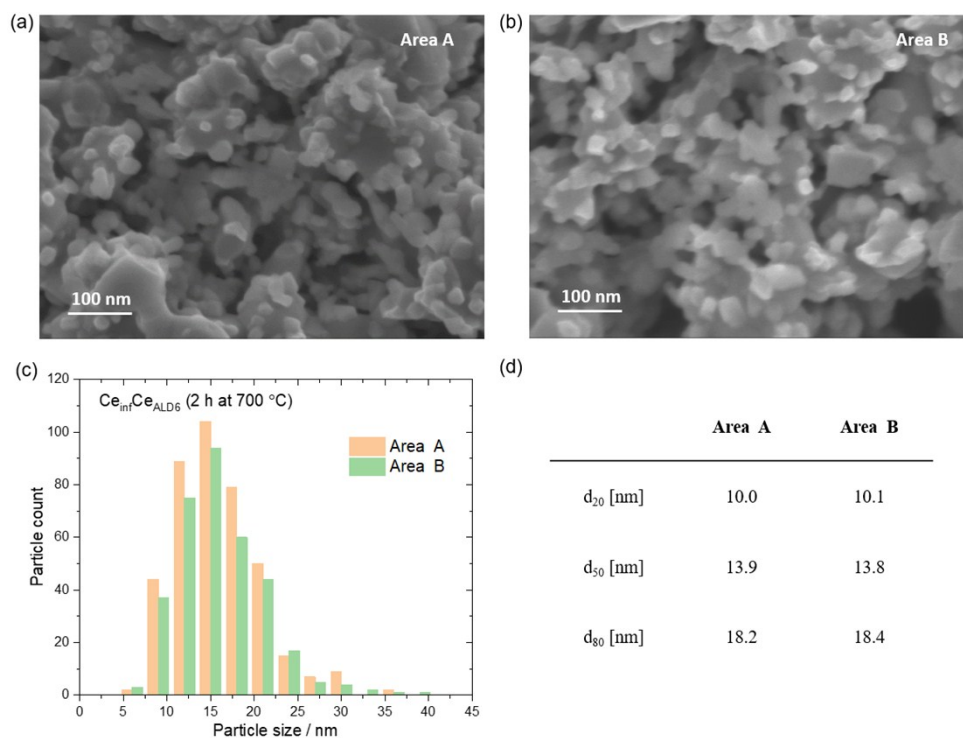


Fig. S11 (a,b) Exemplary SEM images taken from two different areas of a $\text{Ce}_{\text{Inf}}\text{Ce}_{\text{ALD6}}$ sample and the resulting particle size distributions (c) and d_{20} , d_{50} and d_{80} values (d).

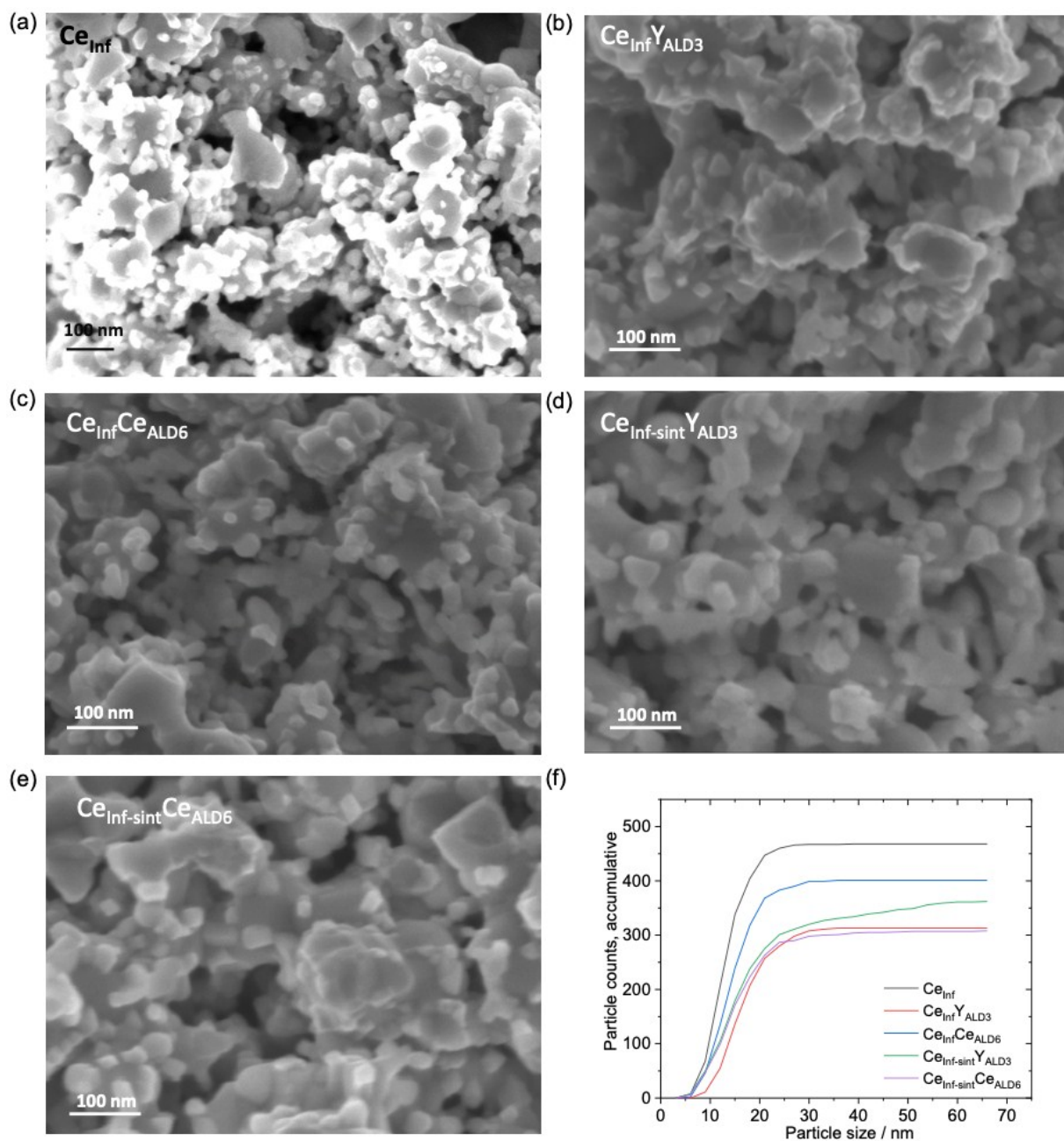


Fig. S12 (a-e) SEM micrographs of 5 different samples at the initial stage of thermal stress (after 2 h at 700 °C). (f) Accumulative number of particles versus particle size, counting from those with smaller particle size.

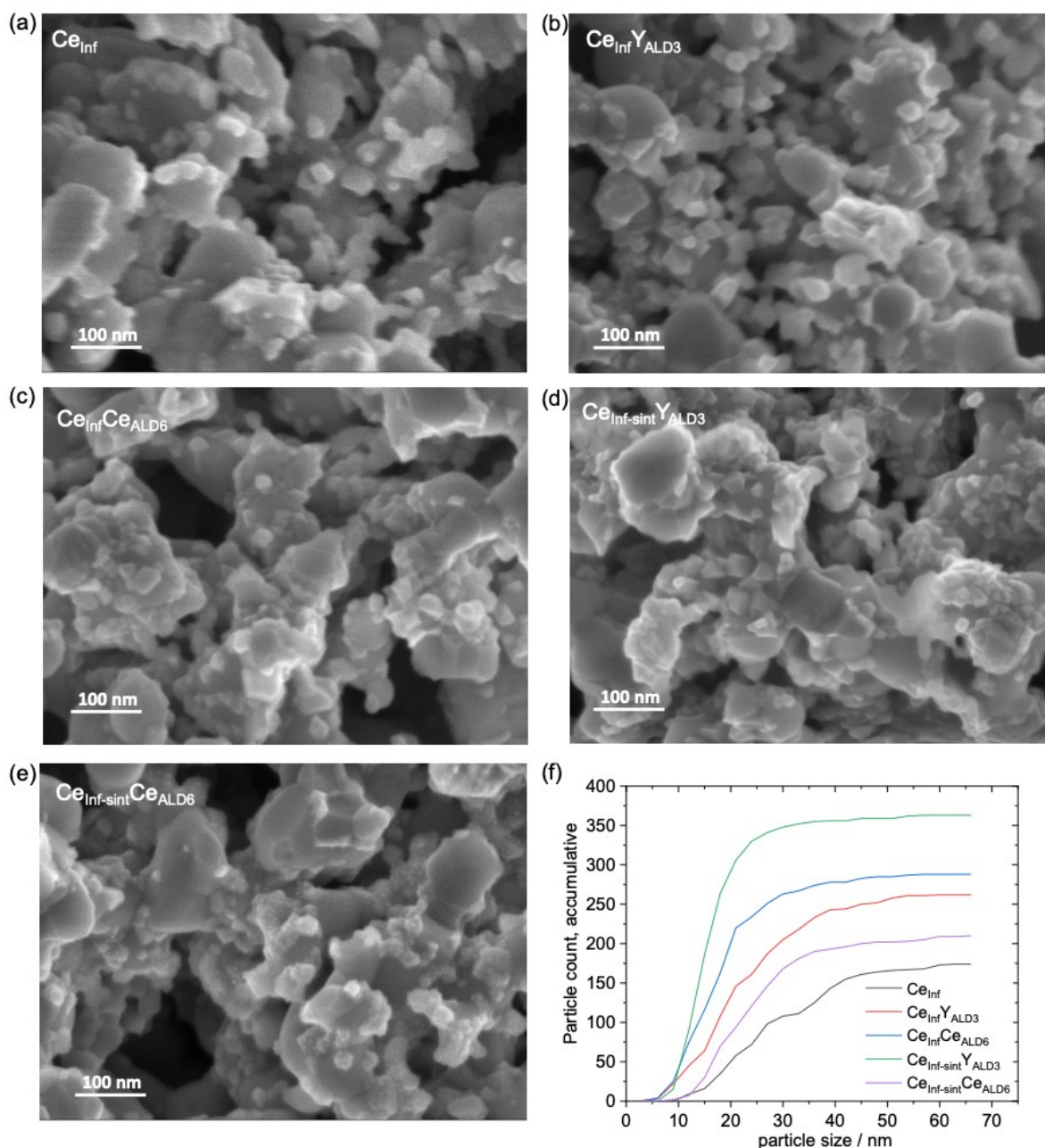


Fig. S13 (a-e) SEM micrographs of 5 different samples after 260 h at 700 °C. (f) Accumulative number of particles versus particle size, counting from those with smaller particle size.

Table S5. Summary of d_{20} , d_{50} and d_{80} values of each sample after 2 h and 260 h at 700 °C.

Samples		d_{20} [nm]	d_{50} [nm]	d_{80} [nm]
Ce_{Inf}	2 h	9.6	12.6	16.7
	260 h	18.0	25.7	38.4
Ce_{Inf}Y_{ALD3}	2 h	12.3	15.9	20.6
	260 h	13.2	19.7	30.1
Ce_{Inf}Ce_{ALD6}	2 h	10.0	13.9	18.2
	260 h	11.0	16.8	24.5
Ce_{Inf-sint}Y_{ALD3}	2 h	10.2	14.7	20.9
	260 h	11.3	15.0	22.2
Ce_{Inf-sint}Ce_{ALD6}	2 h	9.9	14.3	19.8
	260 h	15.9	22.2	30.0

References

- 1 X. Wang, Y. Jin and X. Liang, *Nanotechnology*, 2017, **28**, 505709.
- 2 A. Gupta, T. S. Sakthivel, C. J. Neal, S. Koul, S. Singh, A. Kushima and S. Seal, *Biomater. Sci.*, 2019, **7**, 3051–3061.
- 3 J. W. Shin, S. Oh, S. Lee, J.-G. Yu, J. Park, D. Go, B. C. Yang, H. J. Kim and J. An, *ACS Appl. Mater. Interfaces*, 2019, **11**, 46651–46657.
- 4 M. Rahmanipour, Y. Cheng, T. M. Onn, A. Donazzi, J. M. Vohs and R. J. Gorte, *J. Electrochem. Soc.*, 2017, **164**, F879–F884.
- 5 J. Niinistö, M. Putkonen and L. Niinistö, *Chem. Mater.*, 2004, **16**, 2953–2958.
- 6 J. H. Shim, C. Chao, H. Huang, F. B. Prinz, S. U. V, R. V April, V. Re, M. Recci and V. May, *Chem. Mater.*, 2007, **19**, 3850–3854.
- 7 P. De Rouffignac, J. S. Park and R. G. Gordon, *Chem. Mater.*, 2005, **17**, 4808–4814.
- 8 K. I. Maslakov, Y. A. Teterin, A. J. Popel, A. Y. Teterin, K. E. Ivanov, S. N. Kalmykov, V. G. Petrov, P. K. Petrov and I. Farnan, *Appl. Surf. Sci.*, 2018, **448**, 154–162.
- 9 H.-S. Kang, S. Grewal, H. Li and M. H. Lee, *J. Electrochem. Soc.*, 2019, **166**, F255–F263.
- 10 J. Y. Chen, J. Rebello, V. Vashook, D. M. Trots, S. R. Wang, T. L. Wen, J. Zosel and U. Guth, *Solid State Ionics*, 2011, **192**, 424–430.
- 11 M. Bevilacqua, T. Montini, C. Tavagnacco, E. Fonda, P. Fornasiero and M. Graziani, *Chem. Mater.*, 2007, **19**, 5926–5936.
- 12 R. A. Budiman, T. Miyazaki, S. Hashimoto, T. Nakamura, K. Yashiro, K. Amezawa and T. Kawada, *J. Electrochem. Soc.*, 2015, **162**, F1445–F1450.
- 13 E. P. Murray, T. Tsai and S. A. Barnett, *Solid State Ionics*, 1998, **110**, 235–243.
- 14 J. Van Herle, A. J. McEvoy and K. R. Thampi, *Electrochim. Acta*, 1996, **41**, 1447–1454.
- 15 Y. Gong, X. Li, L. Zhang, W. Tharp, C. Qin and K. Huang, *J. Electrochem. Soc.*, 2014, **161**, F226–F232.
- 16 Y. Takeda, *J. Electrochem. Soc.*, 1987, **134**, 2656.
- 17 E. Perry Murray, *Solid State Ionics*, 2001, **143**, 265–273.